Seismic Vulnerability of Offshore Wind Turbines to Pulse and Non-Pulse Records

Ahmer Ali [1], Raffaele De Risi [1], Anastasios Sextos [1,2], Katsuichiro Goda [3], and Zhiwang Chang [4]

[1]Department of Civil Engineering, University of Bristol, United Kingdom

[2]Aristotle University of Thessaloniki, Greece

[3]Departments of Earth Sciences and Statistical and Actuarial Sciences, Western University, Canada

[4]Department of Civil Engineering, Southwest Jiaotong University, China

The increasing number of wind turbines in active tectonic regions has attracted scientific interest to evaluate the seismic vulnerability of offshore wind turbines (OWTs). This study aims at assessing the deformation and collapse susceptibility of 2 and 5-megawatt OWTs subjected to shallow-crustal pulse-like ground motions, which has not been particularly addressed to date. A cloud-based fragility assessment is performed to quantify the seismic response for a given intensity measure and to assess the failure probabilities for pulse-like and non-pulse-like ground motions. The first-mode spectral acceleration $S_a(T_1)$ is found to be an efficient response predictor for OWTs, exhibiting prominent higher-mode behavior, at the serviceability and ultimate conditions. Regardless of earthquake type, it is shown that records with strong vertical components may induce nonlinearity in the supporting tower, leading to potential failure by buckling in three different patterns: (i) at tower base near platform level, (ii) close to tower top, and (iii) between the upper half of the main tower and its top. Type and extent of the damage are related to the coupled excitation of vertical and higher-lateral modes, for which tower top acceleration response spectra $S_{a,i(T\mathrm{op})}$ is an effective identifier. It is also observed that tower's slenderness ratio (l/d), the diameter-to-thickness ratio (d/t) and the rotor-nacelle-assembly mass (m_{RNA}) are precursors for evaluating the damage mode and vulnerability of OWTs under both pulse-like and non-pulse-like ground motion records.

KEYWORDS
offshore wind turbines, seismic vulnerability, pulse-like records, vertical component, collapse limit, buckling

1. INTRODUCTION

Wind energy has emerged as a reliable source of sustainable power generation by harnessing a plenitude of kinetic energy from strong, yet favorable, wind conditions. The phenomenological conversion of the moving air into electricity is performed by wind turbines, generally, comprising of a rotor-nacelle-assembly (RNA) mounted upwind over a cylindrical slender steel tower. In case of onshore wind turbines, the tower base is fixed at the ground surface, but for most of the offshore cases the tower extends further into the seabed. Wind turbines of different scales have already been deployed around the globe at various onshore locations of ample wind density [1]. However, offshore sites have greater potential due to abundant wind resources, large available space for wind farms, and suppressed noise issues. For these reasons, offshore wind turbines (OWTs) have been particularly popular in non-seismic parts of Europe, where wind and wave-induced loads are the key design drivers for OWTs. The installed wind power continues to grow worldwide, where many countries are developing and investing in the offshore wind energy including those located in the high seismic zones [2], some examples include the planned Morrro Bay offshore wind farm (California), the installed Butera offshore wind farm (Italy), etc.

A plethora of research has focused on the dynamic behavior of OWTs, caused by (i) aerodynamic interaction between the rotor and wind, (ii) hydrodynamic interaction of sea waves with the support structure, (iii) operational vibrations, and (iv) dynamic soil-pile interaction. The latter causes changes in dynamic soil stiffness and damping, in turn, affecting the design frequency of the whole turbine system. Moreover, in active tectonic regions, such as the United States, China, Japan, India, and Southern Europe, strong earthquakes may affect the design of wind turbines under coupled and/or uncoupled effects of wind, wave and seismic loads, considering various operational states [3–8]. Existing design guidelines suggest seismic quantification of wind turbines using response spectra or acceleration time histories [9–11]. In the latter case, seismic inputs should be consistent with regional seismicity and seismotectonic characteristics. As shown in [12], a 2-megawatt (MW) monopile-supported OWT is vulnerable to extreme un-scaled crustal and interplate earthquakes, however, the influence of pulse-like records was not investigated.

In near-fault regions, ground motions have long been known to inherit velocity pulses of large amplitude, being distinctly different from far-field ground motions [13–15]. In case of a 1.5MW onshore wind turbine, Sadowski et al. [16] showed near-fault records with pulse-like effects more damaging than far field records. Near-fault pulses are produced either due to forward propagation of the fault rupture towards the site, i.e., directivity effects [17], or fault displacement due to rupture, known as fling-step effects [18]. Such records are of interest to seismologists and engineers, as they expose structures to a large amount of seismic energy in a short duration, therefore, structures are imposed to severe seismic demand [13]. The classification of pulse-like ground motions has been studied by determining the controlling parameters through wavelet and energy-based algorithms [14,15,19–21]. The velocity pulse period T_p is identified as the key parameter to influence the elastic and inelastic responses of single and multi-degree-of-freedom systems [22–26]. In case of structures that are sensitive to higher modes, pulse-like records with $T_p/T_1 \leq 1$ may impose critical damage at the top stories of tall buildings [27–29], where T_1 is their first natural period of vibration.

In the context of performance-based earthquake engineering, the choice of an appropriate intensity measure (*IM*) is important to characterize the engineering demand parameters (EDP) for structures that may exhibit inelastic behavior [30]. For conventional structures, the first-mode spectral acceleration, $S_a(T_1)$, is often deemed an efficient *IM* to predict the response with reasonable accuracy. However, the suitability of $S_a(T_1)$ has been debated for cases where structural dynamics involve high-mode behavior, and thus, various *IMs* (elastic, inelastic, structure-specific and non-structure specific, scalar and vector) are suggested in the literature [31–33]. In view of pulse-like records, Kohrangi et al. [34] reported the efficiency and sufficiency of T_p/T_1 in predicting deformation and acceleration responses of 2- to 20-storey buildings, and also, showed the average spectral acceleration (*AvgSA*) to be a better proxy of spectral shape than $S_a(T_1)$. *AvgSA* is the geometric mean of spectral values in the range [T_2, $2T_1$], where T_1 ranges from 0.87 to 2.85s and T_2 is the second period of vibration.

Unlike conventional buildings, OWTs support significant structural mass at the top in the form of an RNA. The fundamental period (T_1) of wind turbines can be comparable to tall buildings; for high-capacity multi-MW machines located offshore and supported on monopile-foundations, T_1 can even reach 4.0s. Moreover, discrete mass contributions of the tall slender tower, nacelle, hub, and blades, inducing rotary inertia effects at the tower, can elongate higher modes of vibration [35]. To avoid complexity and high computation cost in numerical models, RNA details including the rotary inertia are often neglected and approximated as total RNA mass atop the tower. In this regard, De Risi et al. [12] incorporated the RNA rotary inertia into the numerical model of a 2MW-OWT, and investigated its performance to near- and far-field records without any particular consideration to pulse-like records. Their results showed that $S_a(T_1)$ can be a sound predictor of excessive deformation and collapse in monopile-supported OWTs.

The interplay of long-period nature of OWTs and pulse-like ground motions may result in major structural damage of OWTs, and to date, this has not been properly addressed in the literature. The present study aims at filling this research gap by scrutinizing an efficient choice of intensity measure (*IM*), and by investigating the seismic vulnerability of two different size OWTs using the performance-based earthquake engineering approach. Extensive sets of crustal pulse-like and non-pulse like records are employed to assess the structural performance of OWTs at serviceability and ultimate limit conditions, using nonlinear dynamic analyses. An improved energy-based algorithm, following [21], is adopted for the pulse classification. This method classifies a record as pulse-like if the predominant velocity pulse contains at least 34% of the total seismic energy. Prior to the pulse and non-pulse classification, the peak ground velocity (*PGV*) is used as a criterion to avoid the inclusion of low-amplitude ground motions into the selected bin of records [14]. Novel contributions of this paper include the systematic and detailed examinations of the velocity pulse effects on different size OWTs and the quantitative evaluations of their structural performances via cloud-based fragility analysis [36]. The cloud results are explored to underpin the causative mechanism that may lead to the tower buckling in OWTs. Various tower damage modes are identified by assessing the contribution of strong vertical ground motions, through the shear and compressive stress variation across the tower and acceleration response at the nacelle. Four parameters; the tower top spectral response $S_{a,i(Top)}$, the RNA mass m_{RNA}, the tower slenderness ratio (l/d), and the diameter-to-thickness ratio (d/t), are observed to be efficient precursors for evaluating the damage modes and their locations, and the seismic vulnerability of OWTs, with the prominent higher-mode response, under pulse-like and non-pulse like records.

2. CASE STUDIES

2.1. 2MW – Vestas V66

The Vestas V66-2.0 is an industrial offshore wind turbine, located at Blyth Offshore Wind Farm (UK). The geometrical/structural specifications of the RNA, supporting tower, monopile and ground are adopted from [12].

Except for the overall weight, there is no actual information available on the structural features of the RNA of Vestas V66-2.0, either by the manufacturer or in the literature [37]. Hence, blade details including its length, material properties, cross-sections and the location of the nacelle relative to the tower axis are assumed to compute the rotary inertia of the RNA.

2.2. 5MW – NREL Reference Wind Turbine

The reference specifications of the NREL offshore 5MW baseline wind turbine are adopted [38]. Complying to the schematics used in Offshore Code Comparison Collaboration (OC3) project [35], the supporting tower is placed atop a constant diameter tubular steel monopile, reaching mudline 20m below the mean sea level (MSL). The subsoil portion of the monopile is embedded 36m deep in an assumed homogenous soil profile. The geometrical and mechanical details of both wind turbines used in this study are listed in Table 1.

TABLE 1 Geometrical and mechanical details of OWT cases

		Symbol	Rating		Unit
			2MW	5MW	
Rotor-Nacelle-Assembly (RNA)					
Mass of the rotor		m_{Rot}	23	121.3	ton
Mass of the nacelle		m_{Nac}	57	264.5	ton
Mass of the RNA		m_{RNA}	80	386.8	ton
Rotor diameter		d_{Rot}	70	126	m
Blade length		r_B	35	61.5	m
Blade mass		m_B	3.36	19.56	ton
Hub diameter		d_{Hub}	-	3	m
Hub height above MSL		h_{Hub}	73	90	m
Supporting tower					
Main Tower	Height above MSL	h_T	54.5	77.6	m
	Bottom diameter	d_B	4.25	6.00	m
	Top diameter	d_T	2.75	3.87	m
	Bottom wall thickness	t_B	-	27	mm
	Top wall thickness	t_T	-	19	mm
	Average wall thickness (chosen)	t_{avg}	34	(30)	mm
Substructure	Transition piece above MSL	$l_{Tp,a}$	16.5	10	m
	Transition piece below MSL	$l_{Tp,b}$	16.5	20	m
	Platform height above seabed	$h_p=l_{Tp,a} + l_{Tp,b}$	33	30	m
	Embedded monopile length	l_M	15	36	m
	Diameter	d_M	3.5	6.00	m
	Thickness	t_M	50	60	mm
Total height		$H = h_T + h_P + l_M$	102.5	143.6	m
Effective tower unit weight		γ_T	78.50	85.00	kN/m^3
Tower's Young's modulus		E_T	210	210	GPa
Tower's shear modulus		G_T	80.8	80.8	GPa
Tower's Poisson's ratio		ν_T	0.3	0.3	-
Geotechnical properties					
Soil's unit weight		γ_s	18.5	10	kN/m^3
Soil's shear modulus at pile tip		G_s	250	250	MPa
Soil's Poisson's ratio		ν_s	0.25	0.25	-
Soil's internal friction angle		φ'	35	35	degree

3. NUMERICAL MODELING

The natural frequency of the two wind turbines differs with the stiffness and mass of the tower-foundation system and the RNA. This study considers two wind turbines of different capacities, i.e. (a) 2MW and (b) 5MW, to examine the variations in their seismic performances. A set of 80 pulse-like and 80 non-pulse-like un-scaled records is used for nonlinear dynamic analysis. The ground motions are applied in all three directions, leading to a total of 480 time-history analyses for each wind turbine case. The details on these two turbines are discussed in the following section.

3.1. Structural modeling

The structural models of OWTs are developed using OpenSees software [39]. The supporting tower includes the main tower, the transition piece, and the monopile, and it is modeled using displacement-based beam-column elements, which allow the progression of nonlinearity along the element length. The cross-sectional non-uniformity of the main tower with height is catered through non-prismatic section models defined with three integration points along each element. The hollow circular fiber sections are utilized for the supporting tower. Each section constitutes 4 fibers along the thickness and 1,000 fibers along the perimeter. Eight points are used to monitor element outputs at each node, e.g. stress and strain. The presence of internal stiffeners, doorway and manufactural imperfections are ignored in this study, which may lead to slight underestimation of the effects [12,16]. The supporting tower is discretized using the Bartdof curvature parameter for thin cylindrical shells [40], such that the elements behave as intermediate shells with their cross-sectional strength limit dominating the buckling behavior. The sub-soil portion of the supporting tower, i.e. monopile, is modeled as a beam on lateral nonlinear-Winkler foundation using displacement-based beam elements. The springs are spread along the pile length according to its discretization, as shown in Figure 1(a). The springs' constitutive behavior is characterized using p-y, t-z, and Q-z springs [41–43]. The input properties to simulate the lateral and vertical mechanical behavior of soil springs include soil's unit weight, internal friction angle, and shear modulus, as listed in Table 1. Figure 1(b) shows the idealized schematics of the soil-pile interaction model.

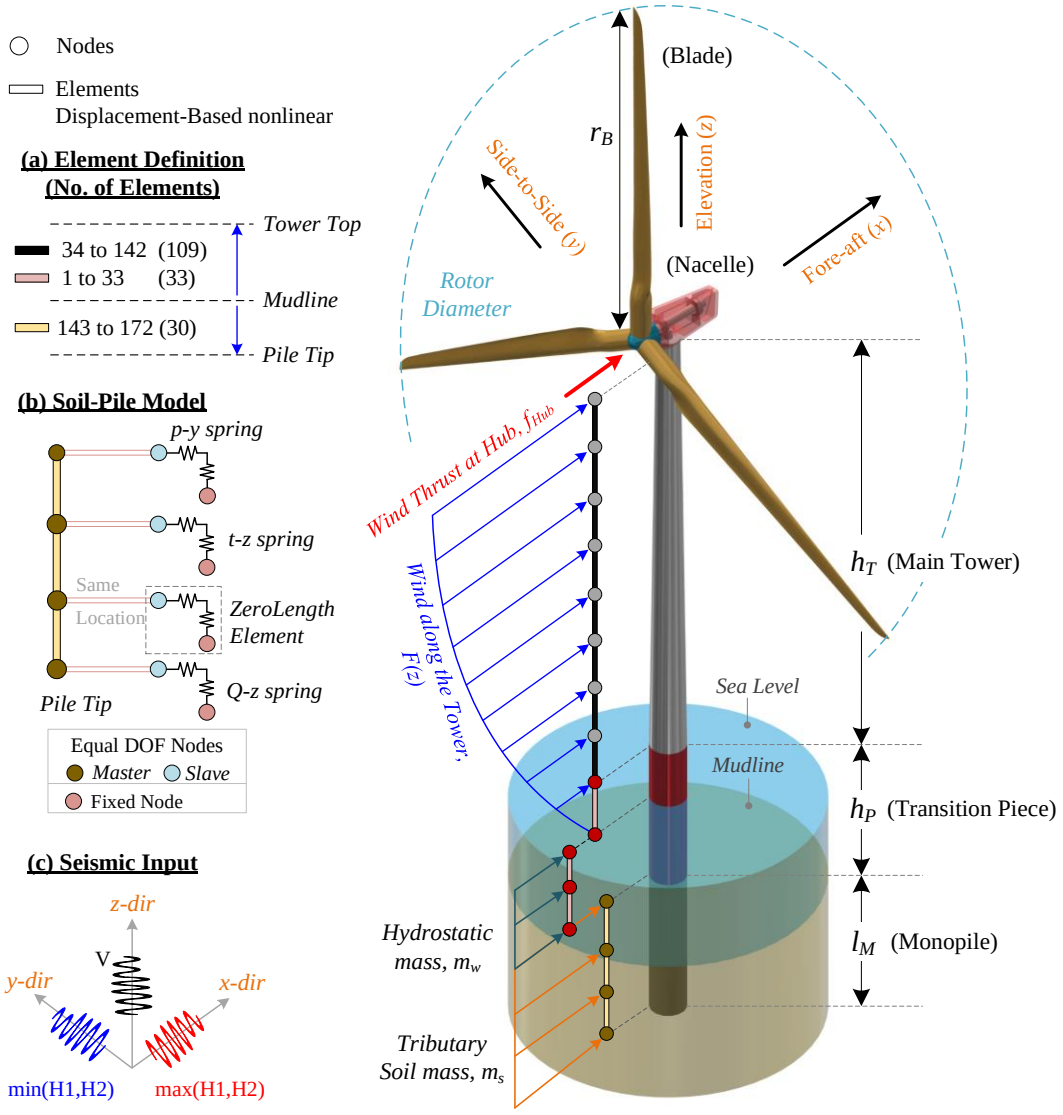

FIGURE 1 Schematic representation of OWT model geometry, wind loads, soil-water mass; (a) element definition; (b) geotechnical model; and (c) earthquake input directions

3.2. Load considerations

Since the primary focus of this study resides in investigating the effects of pulse-like ground motions, the dynamic complexity arising from the rotor operation, aerodynamic, and hydrodynamic loads are idealized. The dynamic force due to rotor vibrations is neglected, while wind loads are statically applied along the tower and at the hub, as shown in Figure 1. Wave loads are applied as nodal masses, assuming stationary sea-conditions, whereas the earthquake loads are modeled in the dynamic regime. All these loads are discussed in the following sub-sections.

3.2.1. Vertical/inertial loads

The total structural weight is obtained as the sum of the masses of individual components, namely the RNA mass (m_{RNA}), the mass of the tower above the MSL, the mass of the transition piece above and below the MSL, and the mass of the monopile. The turbines are installed at the water depth equivalent to $l_{Tp,b}$, listed in Table 1. As water follows the motion of the body, the effect of water inertia needs to be modeled with the body as hydraulic added mass [44]. Assuming stationary wave conditions, the inertial component of the water load is incorporated into the structural mass of the submerged part of the transition piece (m_w=0.8×$m_{TP,sub}$). Moreover, the effect of tributary soil mass inside and around the hollow monopile is considered for an amount equivalent to the pile dimensions. All masses are applied to the structural nodes. Given the lack of actual rotor details of V66-2.0, a fiberglass blade of length (r_B) of 35m and a mass (m_B) of 3.36 ton are adopted [12] to estimate the rotational inertia of blades acting at the center of the swept area, also known as, the barycenter of blade masses. For seismic analysis, relevant guidelines [11] suggest RNA mass atop the tower. However, in reality, the rotor is eccentric to both nacelle and tower yaw axis, where the nacelle center of mass (CM_N) can as well be vertically and/or laterally misaligned from the yaw axis. In this study, CM_N is assumed to coincide with the tower top connection node (T_C) and the rotor inertia is transferred at T_C by an amount of ex_b using the Steiner's principle. Thus, the total mass is lumped at T_C with a given vertical eccentricity $e_{z,c}$ only. The schematics of RNA inertia are presented in Figure 2 and Table 2.

TABLE 2 RNA location and orientation

	2MW	5MW	Unit
Rotor orientation, shaft tilt (θ)	Upwind, 0˚	Upwind, 5˚	deg
Coordinate location of CM_N (e_x, e_y, e_z) from yaw axis	(0,0,2)	(0*,0,1.75)	m
Vertical distance from yaw bearing to shaft ($e_{z,c}$)	2	1.9626	m
Distance from rotor center CM_R to T_C (ex_b)	3	5	m

**assumed value; actual value of e_x = -1.9 m* [38]

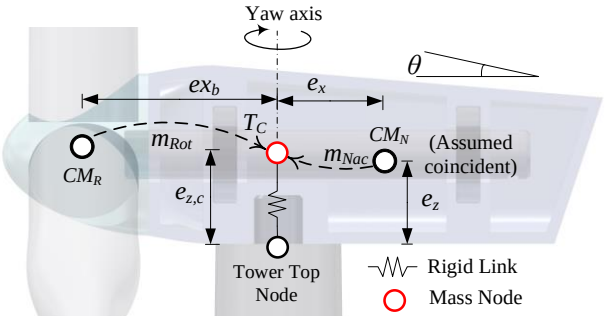

FIGURE 2 Schematics for RNA inertia; rotor and nacelle mass transferred at the shaft location with vertical eccentricity only

3.2.2. Wind loads

Following ASCE/SEI [45] and IEC [9], the normal wind profile model (NWP) is employed to calculate the wind speed variation with the tower height. Assuming the standard wind turbine class, the normal wind speed profile is given by the power law, defined in Equation (1) and transformed into horizontal forces using Equation (2):

$$V(z) = V_{Hub} \cdot \left({}^{z}/_{h_{Hub}}\right)^{\alpha} \quad (1)$$

$$F(z) = 0.5 \cdot \rho_a \cdot V(z)^2 \cdot A(z) \quad (2)$$

where $V(z)$ is the mean wind speed; V_{Hub} corresponds to the reference wind speed, i.e., 15 m/s, acting at the center of the rotor/hub (CM_R) [46]; z reflects tower elevation; h_{Hub} is turbine's hub height above the MSL as listed in

Table 1; and α is the wind shear or power law exponent, taken as 0.2. Moreover, $F(z)$ refers to transformed nodal wind forces; ρ_α is the air density, taken as 1.25 kg/m^3; and $A(z)$ reflects the tributary area of the elements. The impact of thrust forces on the RNA is also considered using a simplistic approach as follows [47]:

$$f_{Hub} = 0.5 \cdot \rho_{air} \cdot V_{Hub}^2 \cdot (\pi \cdot R_T) \cdot C_T \quad (3)$$

$$C_T = 3.5 \cdot V_r \cdot (2 \cdot V_r + 3.5)/V_{Hub}^3 \quad (4)$$

where f_{Hub} is the wind thrust force on the RNA; R_T is the rotor radius; and C_T refers to the thrust coefficient, approximated in the operational range of wind turbines using rated wind speed V_r by the method outlined in [48].

3.2.3. Earthquake loads

Databases, as well as a classification approach adopted to select input motions for nonlinear dynamic analyses are detailed in Section 4. Ground motions are applied in all three directions, where stronger horizontal component (*PGA*) acts along the wind direction, as shown in Figure 1(c). With approximate geotechnical details, site response and wave propagation effects along the pile [49] are currently deemed unaccountable, thus, input motions are assumed uniform along the monopile spring supports. However, this assumption can underestimate the dynamic response in OWTs, especially for layered soils [6].

3.3. Analysis cases

3.3.1. Eigenvalue analysis

Eigenvalue analyses are performed for model validation and to identify the dynamic characteristics of the two OWTs studied, having different hub heights, rotor diameters, embedded monopile lengths and RNA masses, albeit similar material properties.

3.3.2. Cloud-based fragility analysis

A series of nonlinear dynamic analyses are performed to assess the seismic vulnerability of OWTs under unscaled pulse-like and non-pulse-like ground motions. The results are obtained through the cloud-based approach to assess the exceedance of a limit state in terms of an engineering demand parameter (EDP) given an intensity measure (*IM*). EDP is expressed as the scalar critical demand (D) to capacity (C) ratio $\{Y_i=D_i/C_i,\ i = 1{:}\ n\}$, equal to unity, obtained through nonlinear time-history analysis for n ground motions; detailed in the following section. The cloud analysis benefits from a probabilistic linear regression model. The regression scheme fits the calculated response variable to a selected *IM*. The parameters of the regression model are used to quantify the efficiency of an *IM*. Based on the cloud analysis results, the fragility curves of OWTs are derived and expressed as the probability of $Y > 1$ at a given *IM* as follows [36]:

$$P(Y > 1|IM) = \Phi\left(\frac{\log_{10}\eta_{Y|IM}}{\beta_{Y|IM}}\right) \quad (5)$$

$$\log_{10}\eta_{Y|IM} = \log_{10} a + b\log_{10} IM \quad (6)$$

$$\beta_{Y|IM} = \sigma_{\log_{10} Y|IM} = \sqrt{\sum_{i=1}^{n}\left(\log_{10} Y_i - \log_{10}\eta_{Y|IM}\right)^2/(n-2)} \quad (7)$$

where $P\,(Y > 1|IM)$ defines the structural fragility as the probability of an EDP exceeding a prescribed limit given an *IM*. The terms $\log_{10}\eta_{Y|IM}$ and $\beta_{Y|IM}$ are the logarithmic mean and standard deviation of Y at a given *IM*, respectively. $\Phi(\bullet)$ is the standard normal cumulative distribution function. $S_a(T_1)$, *PGA*, and *PGV* are chosen as potential *IM*s. $S_a(T_1)$ is taken as the geometric mean of two horizontal ground motion components, whereas *PGA* and *PGV* are represented as the geometric mean of all three components.

3.4. Performance criteria

For structure-foundation integrity, code provisions require multiple performance checks, mainly concerned with the ultimate capacity and serviceability of structures. Adhering to codified guidelines [9–11] and recently acknowledged literature [12,50,51] on the subject matter, the following performance limit states are checked for evaluating the seismic vulnerability of OWTs.

3.4.1. Serviceability limit state (SLS)

Det Norske Veritas (DNV) guidelines [10] suggest a threshold of ±0.5˚ for the maximum (i.e., allowable) monopile rotation at the mudline below the sea level. Notably, no criteria exist in the codes regarding the tower

top rotation, which may enhance the performance and design of OWTs, and its evaluation is beyond the scope of this study. Given their height-dependent cross-sectional properties, the monopile, the transition piece, and the main tower are modeled as a continuum by defining varying, yet equivalent, nodal kinematics. Thus, a maximum tower top rotation of ±0.5˚ is assumed as the permissible limit to ensure the SLS criteria [12,50].

3.4.2. Ultimate limit state (ULS)

The ULS follows EN 1993-1-6 [52] to verify the strength and stability of the supporting towers of the OWTs under study. The ULS demand (D) to capacity (C) ratio is taken as the maximum of Equation (8) and (9), where σ and τ are the meridional and planar shear stresses, respectively, obtained through OpenSees [39]. The τ-values are taken as the sum of shear and torsional stresses, following Jourawski theory of shear and Bredt theory of torsion for thin-walled circular sections [12,53]. f_y is the yield strength = 355 MPa for S355 steel. For more details on the calculation of $\sigma_{x,Rd}$, $\tau_{x,Rd}$, k_x, and k_τ refer to Part 1-6 of the Eurocode 3 and its Annex D [52].

a. Von-Mises equivalent design stress (σ_{eq})

$$Y = \frac{D}{C} = \frac{\sigma_{eq}}{f_y} = \sqrt{\sigma^2 + 3.\tau^2}/f_y \leq 1 \quad (8)$$

b. Buckling strength check through stress limitation

$$Y = \left(\frac{\sigma}{\sigma_{x,Rd}}\right)^{k_x} + \left(\frac{\tau}{\tau_{x\theta,Rd}}\right)^{k_\tau} \leq 1 \quad (9)$$

4. GROUND MOTIONS FOR DYNAMIC ANALYSIS

4.1. Strong ground-motion data

The seismic input for nonlinear dynamic analysis should represent anticipated earthquake scenarios and must be compatibly selected [54]. For this purpose, a total of 1,243 earthquake records are compiled from the Next Generation Attenuation (NGA) dataset and three Japanese strong-motion networks, namely, K-NET, KiK-net, and SK-net [55]. The compiled dataset corresponds to magnitude (M) range of 5.5 to 9.0, rupture distance (R) up to 200km, *PGA* and *PGV* within 0.1g to 1.75g and 10 cm/s to 110.43 cm/s, effectively covering the entire range of basic ground motion properties. Moreover, it distinguishes among crustal, interplate and inslab earthquakes to assist in categorical selection. These records are further assessed for the presence of velocity pulses, regardless of fault proximity and earthquake type. The pulse identification method adopted in this study is summarized below.

4.2. Pulse identification

A recently proposed energy-based method is adopted for the identification of pulse in the compiled set of ground motions [21]. The proposed method defines the pre-dominant pulse amplitude, in its value and time location, using the half-cycle signal with the largest seismic energy, instead of correlating it to *PGV*, as assumed in the preceding work [20]. The Dickinson and Gavin model [56] is used to eliminate the high-frequency content and extract the predominant pulses from the velocity time histories. The method identifies a record as pulse-like if the extracted velocity pulse contains at least 34% of the total seismic energy. This is achieved by defining a pulse indicator (E_p), i.e., the ratio of relative cumulative energy of the predominant pulse to the total seismic energy.

In this study, a total of 323 out of 1,243 records are identified as pulse-like. These records can be divided into two subsets, i.e., the first set (264 records) entails velocity pulses in at least one of the horizontal components, regardless of the pulse presence in the vertical component, while the second set (59 records) includes ground motions where a predominant pulse is related with the vertical component only. Relevant guidelines [11] associate the tower response, specifically buckling, with two horizontal ground motion components, whereas implications of vertical components are deemed possibly irrelevant. However, the seismic vulnerability of wind turbines to vertical excitations has been recently acknowledged due to high vertical natural frequencies [57], though for a different performance parameter, i.e. nacelle acceleration, which triggers emergency shut-down for a wind turbine if it exceeds a certain threshold [58,59]. To this end, the second subset of records is disregarded from the total pulse-like dataset to avoid the consideration of corresponding non-pulse horizontal components during the selection procedure. However, the sensitivity of tower response to vertical-only velocity pulses in a record, may seem a peculiar case, but not studied explicitly herein.

4.3. Scenario selection

Following the pulse-identification, input ground motions for nonlinear dynamic analysis are prepared from pulse-like and non-pulse-like records (264 and 979, respectively). Figure 3(a) shows three sets of records for response

quantification of OWTs, i.e., Set A, B and C. Set A includes records with strong intrinsic velocity pulses, while Set B and C correspond to non-pulse-like records. A *PGV* limit of 30cm/s is used as a criterion for records involved in the pulse identification [21], to avoid the inclusion of low amplitude ground motions in the selected set of records [14]. Hence, to form a viable comparison with pulse-like records, non-pulse-like records are sub-divided into two sets. Set B contains non-pulse-like records with a mean *PGV* greater than 30cm/s, whereas Set C comprises non-pulse-like records with a mean *PGV* less than 30cm/s. All sets are further categorized based on the earthquake type (crustal, interplate, and inslab) dispersed over magnitude (M) range greater than 6.0 and source-to-site distance of fault rupture (R) up to 100km. In this study, the pulse period (T_p) is neglected in the record classification. However, its effects on the seismic vulnerability of OWTs will be explicitly addressed in the future research. Figure 3(a) reveals the scarcity of pulses in interplate and inslab records, which are insufficient to perform a cloud analysis and are excluded from this study. This can be attributed to the fact that velocity pulses are more prominent in shallow crustal records occurring in near-fault regions.

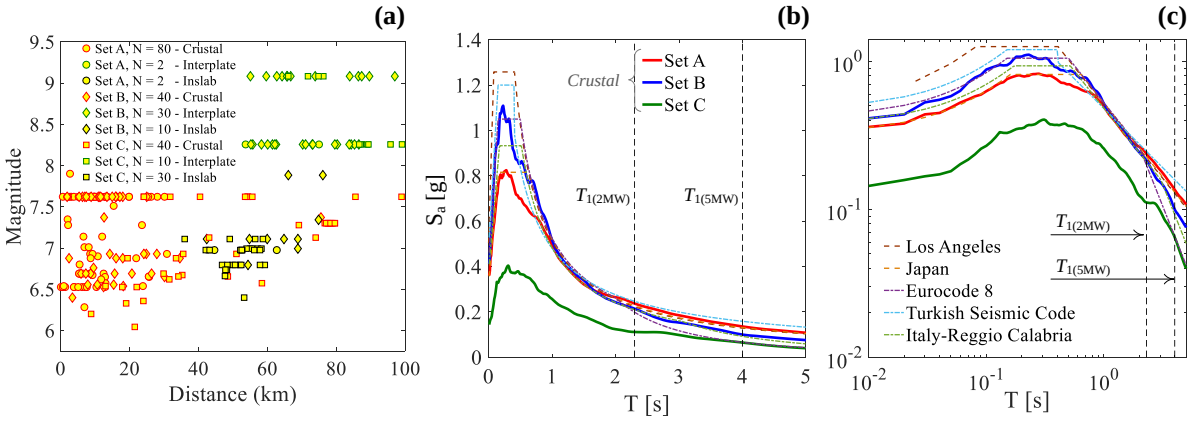

FIGURE 3 (a) Selected record sets; geometrical mean of horizontal response spectra (b) linear; (c) log-scale

The final selection encompasses a total of 160 crustal, 3-component, ground motion records (160 x 3 = 480 acceleration time-histories), comprising 80 pulse-like and a total of 80 non-pulse-like records, as shown in Figure 3(a). Set A, B and C has a mean *PGV* of 58.4cm/s, 48.5cm/s, and 22.0cm/s, respectively. Figures 3(b) and 3(c) portray the mean response spectra of the horizontal crustal ground motions in linear and logarithmic scales, respectively. The uniform hazard spectra (UHS) pertinent to three European, one North American and one Asian seismically active region are considered to check the spectral compatibility of the records. These are potential locations for installed, planned or future offshore wind farms where near-fault crustal grounds motions can be of significance. These include Los Angeles (California) [45], Sendai (Japan) [60], Eurocode 8 [61], Izmir (Turkey) [62], and Reggio Calabria (Italy) [63], considering soil class B and 10% in 50 years probability. The details on the selected sets of records are provided in Table A.1-3 of Appendix. It is noteworthy that for an approximate period range of 0.9s to 2.0s, Set A and B correspond well with the uniform hazard spectra (Figures 3(c)). At long periods, specifically around fundamental periods of the wind turbines (2.3s to 4.0s), Set A spectral accelerations are higher than Set B. However, Set B exhibits larger spectral values at shorter periods than Set A. Moreover, Set A is relatively more coherent with Japanese and Italian spectra, whereas Set B fits the three European spectra more closely. In case of Set C, the overall trend is lower due to weaker ground motion content for *PGV* < 30cm/s, however, 2.5s onwards it matches with the Eurocode 8 spectrum.

5. RESULTS AND DISCUSSIONS

5.1. Modal response

Figure 4 and Table 3 present vibration modes and participation masses of the two OWTs under study. The modal properties of 2MW and 5MW are in good agreement with [12] and [35], respectively. The relative difference between the fundamental periods of 2MW and 5MW OWTs is due to enhanced system flexibility of the latter, consequential to greater tower height, rotor diameter, embedded pile length, and RNA mass as illustrated in Table 1. Table 3 shows similar mass distributions between the two OWTs, however, the amount of mass is relatively less active in the 5MW turbine. In other words, the 2MW turbine requires 16 translational modes to achieve 100%, 100%, and around 90% of mass participation in x, y, and z-direction, respectively. In contrast, the 5MW turbine achieves around 60%, 84% and 88% of mass participation in translational x, y, and z-direction, respectively.

Although similar vertical mass participations are observed in both turbines, the second vertical mode (i.e., mode 13) in the 5MW is activated earlier than the 2MW (i.e., mode 16), at a twice longer vibration period. The missing entries comply with purely rotational modes (e.g. mode 10 in the 5MW) and are omitted herein along with all other rotational modes for brevity. In OWTs, the total damping arises from structural (0.2% to 0.3%), aerodynamic (generally less than 3.5%), hydrodynamic (0.15% or lower), and soil damping combined [10,12,64]. A constant Rayleigh damping of 3% is adopted to account for the total system damping. The affecting modes include the 1st and 6th vibration modes; alike the choice of 1st and 3rd modes for conventional structures as the first six modes are in pairs. Newton-Raphson method is used to solve the system of nonlinear equations [65], where the time increment (Δt) is equivalent to the accelerogram time-step (dt=0.005 or 0.01s), and if required, allowed to reduce iteratively to achieve convergence and the structural response with reasonable accuracy and computational cost. It is noted that the above time-step is adequate to capture the highest mode of interest.

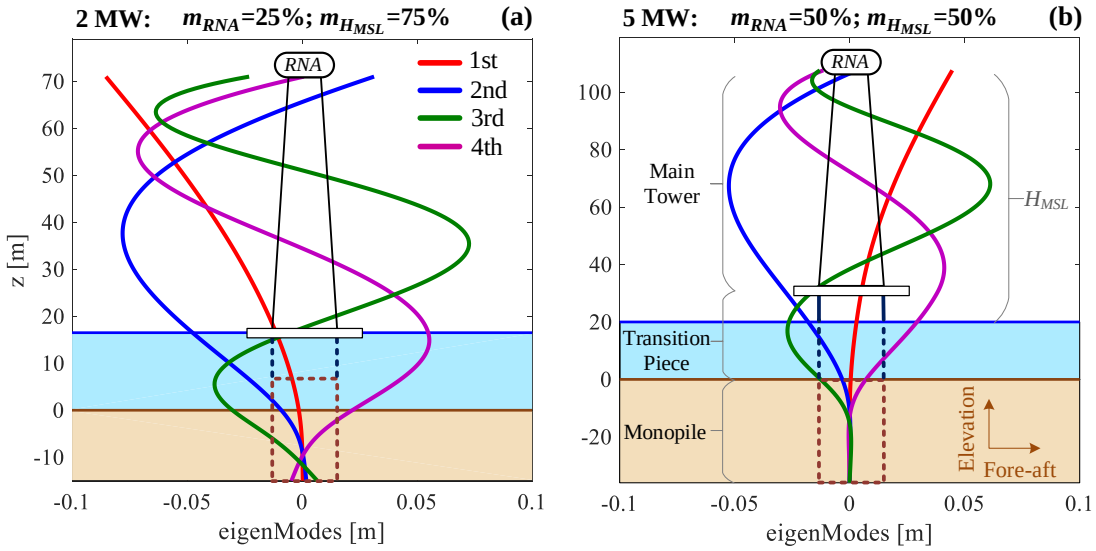

FIGURE 4 First four fore-aft tower bending modes (a) 2MW OWT; (b) 5MW OWT

TABLE 3 Modal frequencies and mass participations

Mode	2MW					5MW				
	T(s)	f(Hz)	Mass participation (%)			T(s)	f(Hz)	Mass participation (%)		
			X	Y	Z			X	Y	Z
1	2.301	0.435	-	21.8	-	4.015	0.249	-	16.6	-
2	2.295	0.436	22.0	-	-	3.979	0.251	17.0	-	-
3	0.414	2.415	-	12.2	-	0.764	1.308	-	6.6	-
4	0.399	2.505	12.9	-	-	0.664	1.506	8.1	-	-
5	0.186	5.386	-	10.3	-	0.364	2.748	-	8.6	-
6	0.172	5.817	11.0	-	-	0.323	3.093	7.6	-	-
7	0.107	9.363	-	8.4	-	0.181	5.519	-	7.6	-
8	0.097	10.289	8.4	-	-	0.175	5.726	7.0	-	-
9	0.080	12.466	-	-	58.9	0.153	6.521	-	-	50.1
10	0.067	14.871	-	19.9	-	0.128	7.814	-	-	-
11	0.065	15.398	21.2	-	-	0.099	10.063	-	6.9	-
12	0.053	18.827	-	25.8	-	0.098	10.173	6.8	-	-
13	0.052	19.103	23.5	-	-	0.068	14.712	-	-	37.5
14	0.045	22.195	-	1.6	-	0.066	15.151	-	13.8	-
15	0.044	22.663	0.9	-	-	0.066	15.206	13.9	-	-
16	0.034	29.242	-	-	29.7	0.052	19.192	-	24.3	-
		∑ =	100	100	88.7		∑ =	60.3	84.4	87.6

5.2. Cloud analysis

The results of the nonlinear dynamic analysis are interpreted through the cloud analysis. Figure 5 shows record-to-record variability for tower deformation of the two OWTs at the SLS versus $S_a(T_1)$, where T_1 for the 2MW

and the 5MW OWT is around 2.3s and 4.0s, respectively, as shown in Table 3. The solid line represents the estimated regression, whereas the dashed lines show a confidence interval corresponding to mean plus/minus one logarithmic standard deviation of the predicted regression. The coefficient a is the ordinate intercept of the regression line; b is the slope of that line; β as described in Equation (7) is the measure of the variability of Y at a given IM and ρ is the Pearson's coefficient that quantifies the goodness of the fit. The value of β in the range of 0.20 to 0.30 shows the efficiency of an IM [66], whereas ρ closer to 1.0 indicates a good fit. The attained demands are normalized to the prescribed capacity, e.g., a maximum tower top rotation of ±0.5˚ for SLS, to illustrate the extent of records exceeding the performance level.

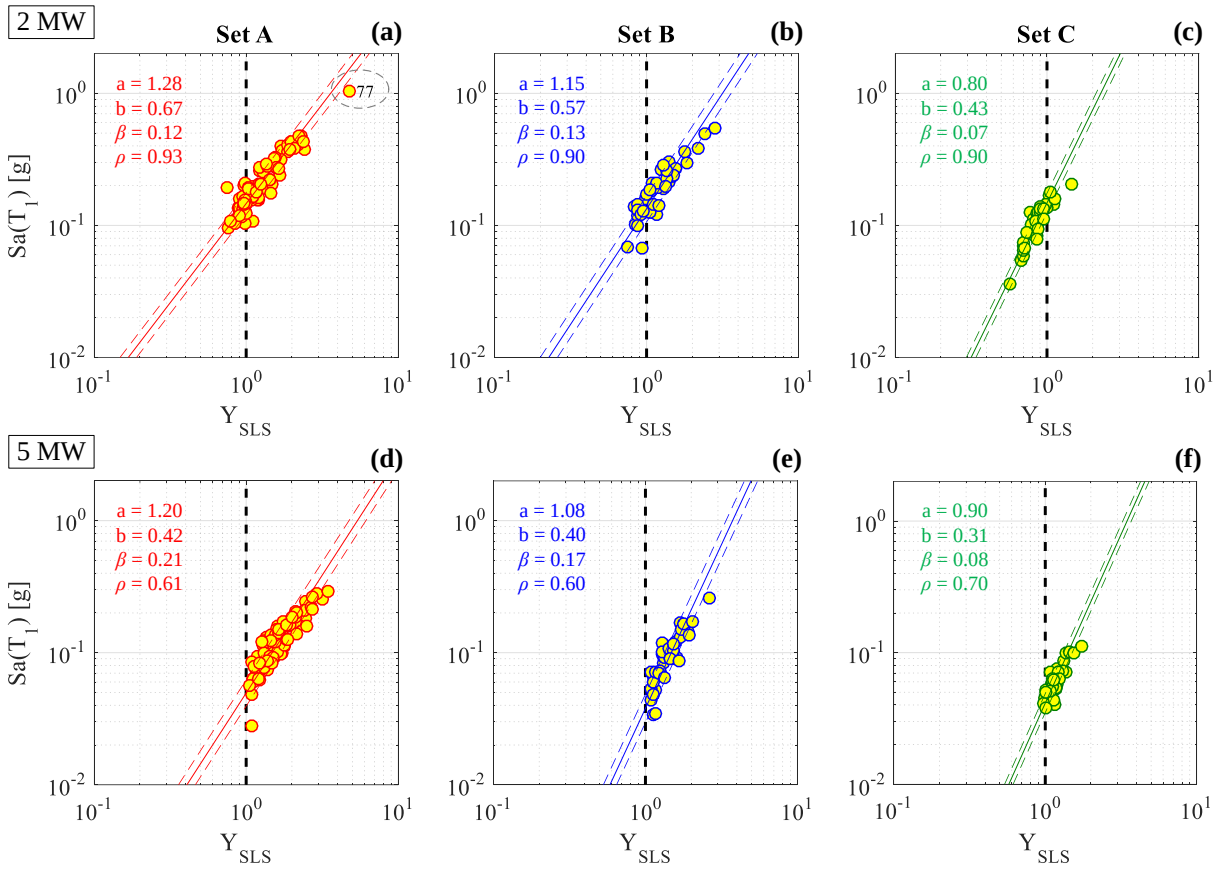

FIGURE 5 Cloud analysis results for $S_a(T_1)$ at SLS

At SLS, all three sets of records have shown low variability for both OWTs, which are susceptible to crustal records regardless of their classification. The OWTs are more prone to deform and exceed the serviceability demand-to-capacity ratio (Y_{SLS}) under pulse-like and non-pulse-like records with a mean PGV > 30cm/s, i.e., Set A and B, respectively. In case of the 2MW OWT shown in Figure 5 (a & b), Set A and B records exceeding Y_{SLS} lie in the spectral range of 0.1g to 0.48g, except for Set A record 77 $S_a(T_1)$ of which reaches 1g. On the other hand, fewer cases of Set C records exceed Y_{SLS} in the spectral range of 0.1g to 0.2g as shown in Figure 5(c). In case of the 5MW OWT shown in Figure 5 (d to f), the tower's SLS limits are likely to be affected by all three sets of crustal records, even for lower $S_a(T_1)$ values and despite the presence of the weaker PGV content in non-pulse-like records (Set C). This behavior, particular to the 5MW, can be associated with the greater tower height and larger RNA mass, i.e., 50% of the total superstructure above MSL. Also, the main tower of the 5MW OWT has a larger cross-section and rotor-swept area, leading to higher static wind forces along the tower from Equation (2) and greater thrust forces on the RNA using Equation (3), respectively. Thus, it may require smaller seismic demand to exceed the SLS capacity for the 5MW OWT.

Figure 6 shows the cloud scatter for the tower's yield and buckling strengths at the ULS, defined by Equation (8) and (9), respectively. At ULS, the record-to-record variability (β) for both OWTs is low and in the acceptable range, i.e., 0.20 to 0.30 [66] as described earlier in this section. In case of the 2MW OWT shown in Figure 6(a), only one pulse-like record with $S_a(T_1)$ around 1g has exceeded the ultimate demand-to-capacity ratio (Y_{ULS}). For non-pulse-like records, only those with stronger PGV content shown in Figure 6(b), have reached

65% to 80% of Y_{ULS} with $S_a(T_1)$ around 0.30g to 0.55g. In case of the 5MW OWT, the dispersion is relatively higher for Set A pulse-like and Set B non-pulse-like records shown in Figure 6(d) and (e), respectively. The OWT has exceeded the Y_{ULS} in an approximate spectral range of 0.08g to 0.30g under Set A and Set B records. The zoomed parts of these figures further reveal that some records have reached higher Y_{ULS} for significantly lower values of $S_a(T_1)$. This may happen due to the absence of the vertical component $S_{a,z}(T_{1,z})$ from the geometric mean of $S_a(T_1)$. In an effort to contemplate the underlying mechanism, the vertical component is incorporated in $S_a(T_1)$, such that the scalar *IM* is formed $S_{a,xyz}(T_1) = \sqrt[3]{S_{a,x}(T_{1,x}) \cdot S_{a,y}(T_{1,y}) \cdot S_{a,z}(T_{1,z})}$. The variability for Set A and B records has decreased in particular with the inclusion of $S_{a,z}(T_{1,z})$ as shown in Figure 6(g) and (h), respectively. Once again, the results are zoomed in to highlight the updated spectral range for which Y_{ULS} has been exceeded. It can be observed that the $S_{a,xyz}(T_1)$ values have increased significantly, such that the spectral values lie in the range of around 0.16g to 0.60g and 0.23g to 0.30g for Set A and B records, respectively. This indicates the presence of strong vertical ground motions in these records and attracts the interest to investigate the governing failure criteria and damage modes for the OWTs.

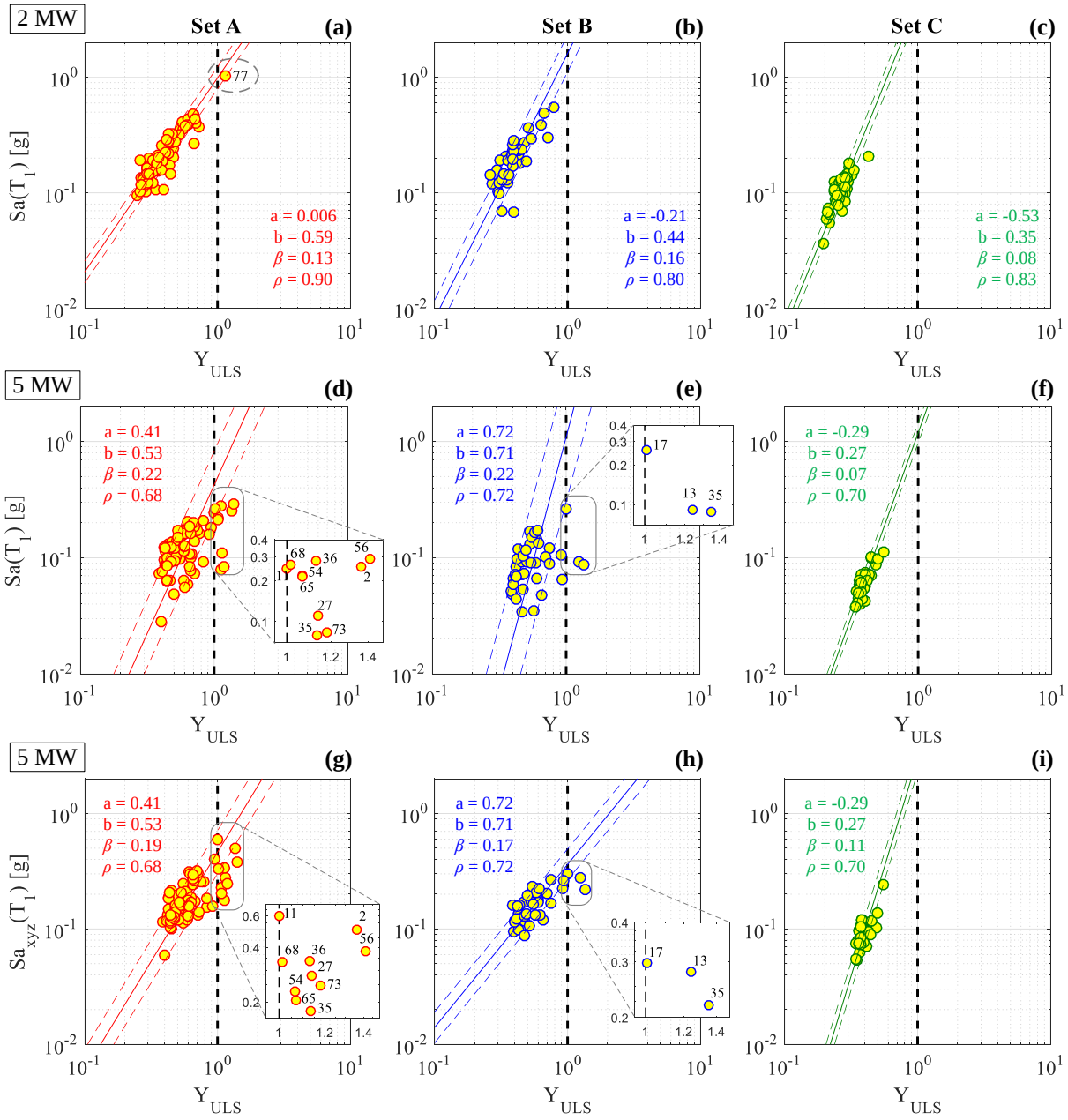

FIGURE 6 Cloud analysis results for $S_a(T_1)$ and $S_{a_{xyz}}(T_1)$ at ULS

In this study, the maximum of the von Mises equivalent design stress and the buckling strength ratio defines the global stability criterion for the OWTs, as described earlier. Figure 7 presents the contribution of these two parameters in achieving the collapse state for the 5MW OWT under Set A and B records. It is apparent that buckling dictates the performance limit for both sets of records. The stress-strain behavior, shear and meridional/compressive stress variation along the supporting tower and the tower top response are further examined to evaluate the governing mechanism and modes of the failure.

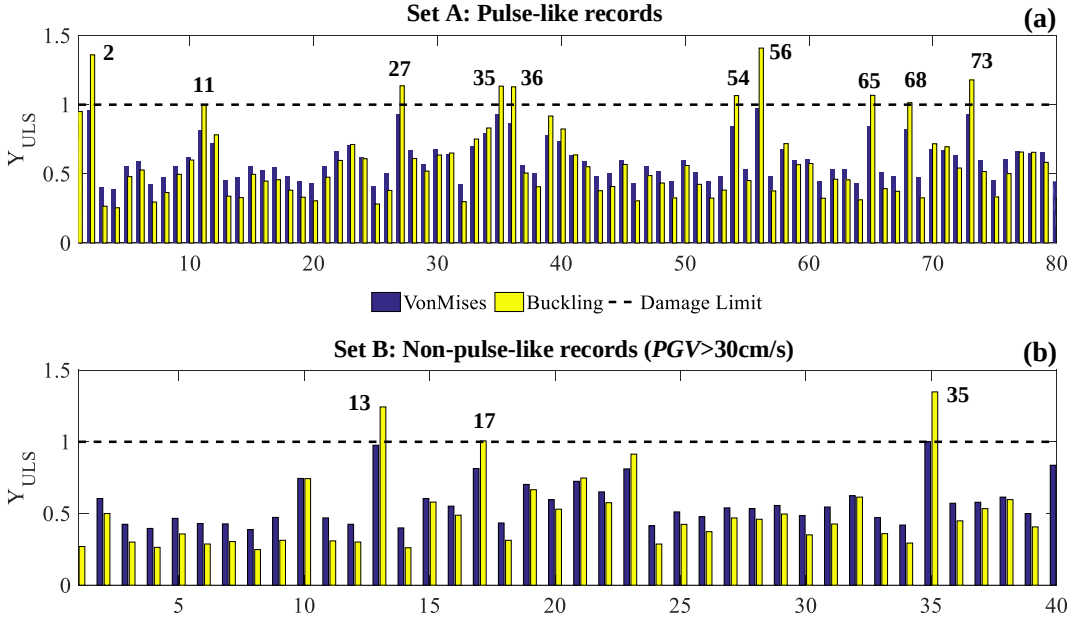

FIGURE 7 Y_{ULS} exceedance of the 5MW OWT by von Mises and buckling stresses (a) Set A; (b) Set B

5.2.1. Stress-strain behavior

The stress-strain (hereinafter referred to as σ-ε) behavior of the turbine tower is assessed to trace the onset of the structural nonlinearity (NL). The asymmetric degrading behavior of the material in compression is an indicator of buckling which is simulated by invoking the negative isotropic hardening (ih = -0.5%) in the material model [67]. Figure 8 shows σ-ε plots of the 5MW OWT tower under those pulse-like (Set A) and non-pulse-like (Set B) records for which the turbine has exceeded the ULS limit. Figure 6(d, e, g & h) presents the numerical index of these records and their spectral values S_a(g) versus Y_{ULS}. Table 4 summarizes the nonlinear σ-ε behavior of the tower and associates its location with the vertical ground motion components in Set A and B records. Figure 8(a to c) shows the progression of slightly to mildly nonlinear σ-ε behavior in the upper half of the tower, i.e., from element 80 to 142 as defined in Figure 1(a). The effect of the material degradation as negative isotropic hardening is mildly prominent in Figure 8(c) under Set A record 73 which contains a significant vertical component as illustrated in Table 4. Similarly, a non-pulse-like record with a strong vertical component, i.e., Set B record 13, causes notable compression instability of the material in the vicinity of the RNA at the tower top shown in Figure 8(f), where Figure 8(e) shows the start of nonlinearity. However, records with weak vertical components, either Set A or B, cause a failure at the tower base near the platform level with a negligible to slightly nonlinear σ-ε behavior shown in Table 4 and Figure 8(d). Thus, it implies that the crustal records with strong vertical ground motions can cause buckling-induced damage in the tower of those OWTs which support 50% of the mass as the RNA.

TABLE 4 Tower nonlinearity for records with varying S_a (g)

IM	Record		S_a(g)	Y_{ULS}	(σ-ε) behavior	Element No.	Location
	Type	No.					
$S_a(T_1)$/ $S_{a,xyz}(T_1)$	Set A	73	0.083/0.246	1.179	Mildly NL	80 - 142	Tower upper half
		36	0.279/0.337	1.129	Slightly NL	34 - 50	Tower base/platform
	Set B	13	0.092/0.279	1.243	Notably NL	125 - 142	Tower Top near RNA
		17	0.261/0.298	1.006	Linear	34 - 50	Tower base/platform

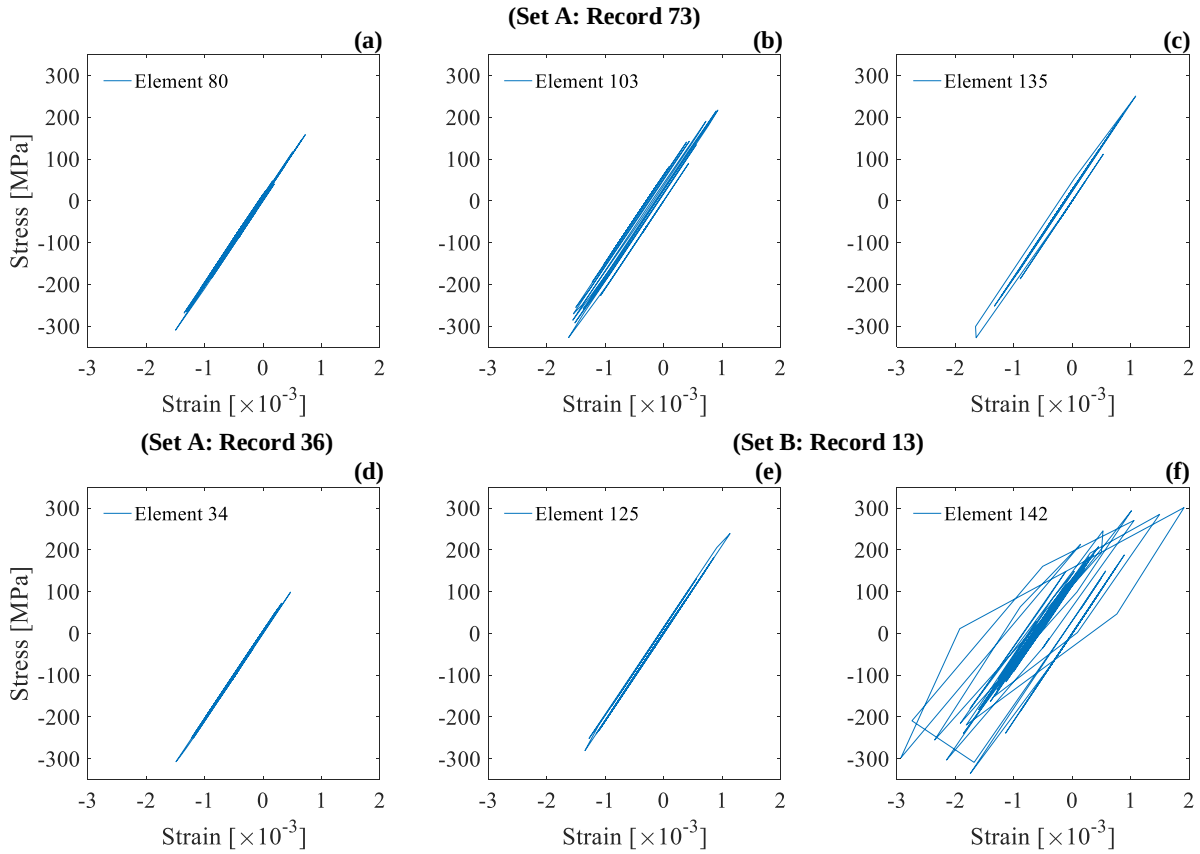

FIGURE 8 σ-ε plots showing progression of nonlinearity and compression instability in 5MW OWT tower due to pulse-like (Set A) and non-pulse-like (Set B) records

5.2.2. Stress variation along the tower

The buckling strength check is performed by examining the meridional (σ) and planar shear (τ) stresses in the hollow cylindrical steel tower, following Annex D of Eurocode 3 [52], described earlier in Equation (9). The meridional stresses cause the longitudinal compression, whereas the planar shear stresses lead to the flexural bending in the tower. The damage modes are further identified by examining the contribution of the compressive and shear stresses along the tower height of the 5MW OWT in Figure 9. Figure 9(a) shows the variation of meridional stress demand ($\sigma_{x,Ed} = \sigma$) and capacity ($\sigma_{x,Rd}$) along the tower. Figure 9(b) plots the changes in planar shear stress demand ($\tau_{x\theta,Ed} = \tau$) and capacity ($\tau_{x\theta,Rd}$) of the tower. Besides a slight variation in the monopile, shear stress demand on the main tower and the transition piece is insignificant. However, the contribution of meridional stresses is prominent in the tower-foundation assembly, indicating buckling by compression as the primary damage mode. Figure 9(c) shows the normalized tower stress (Y_{ULS}) profile under Set A and B records for which the 5MW OWT has reached the ULS, as highlighted earlier in Figure 6 and Table 4. Three different tower profiles, exceeding the ULS limit at three different locations, are observed. These are termed as the damage patterns, and their locations are illustrated in Figure 9(a & c). Damage pattern-1, 2, and 3 corresponds to the failure (1) at the main tower base near the platform, (2) around the tower top, and (3) starting from the upper half till the tower top, respectively. The damage pattern-1 is consequential to the stress concentration due to the thickness difference between the transition piece (60mm) and the main tower (30mm). This agrees with [16,68], where change in thickness led to the formation of plastic hinge at the tower base of a 1.5MW onshore wind turbine, which could spread towards the top and cause failure under extreme earthquake intensities (PGA = 2 to 3g). Thus, the damage pattern-1 may be avoided in OWTs, that are to experience the near-field crustal records with weak vertical components, by controlling the thickness between the substructure and the main tower in the design phase. The diameter of the 5MW OWT tower changes with height, resulting in lower sectional stiffness towards the tower top which supports 50% of the superstructure mass as the RNA. As shown in Table 4, records causing failure near the tower top and the upper half contain significantly high vertical accelerations. Hence, the RNA mass (m_{RNA}) and the cross-sectional geometry of the tower can be the controlling factors for the damage pattern-2 and 3.

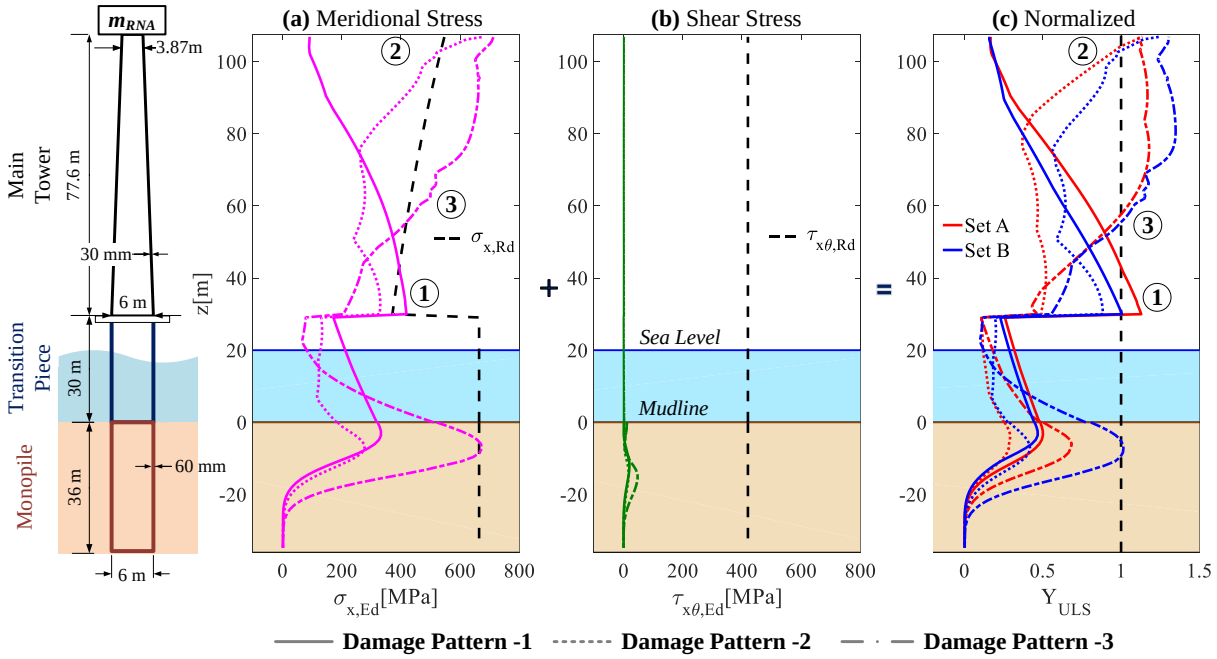

FIGURE 9 Stress and damage variation along the 5MW OWT tower (a) meridional, (b) planar shear, (c) normalized as per Equation (9)

5.2.3. Damage modes and tower top response

Higher mode response is a significant dynamic feature, leading to an increased seismic response at the nacelle of tall large-scale wind turbines [8]. The tower top response $S_{a,i(Top)}$ is examined to associate the damage modes with the modal behavior of the OWTs. Figure 10 shows the tower top response spectra for those pulse-like (Set A) and non-pulse-like (Set B) records that induced failure in the 5MW OWT by the damage pattern-1, 2, and 3.

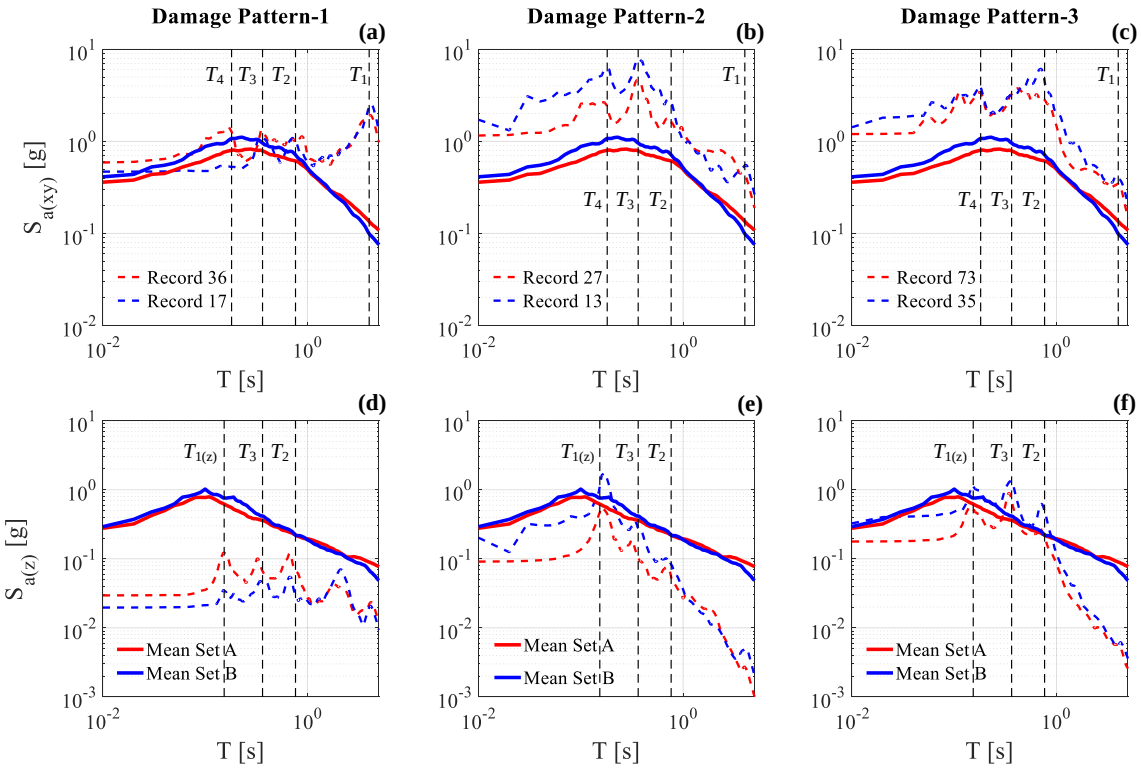

FIGURE 10 Relation between damage patterns and the tower top response spectra (a-c) geometric mean of horizontal components; (d-f) vertical component

Figure 10(a to c) presents the spectral response $S_{a(xy)}$ of the records in comparison with the mean response spectra of Set A and B records, taken as the geometric mean of the two horizontal components. Figure 10(d to f) shows the vertical acceleration response of the records in comparison with the mean vertical response spectra of the Set A and B records. The index of these records is also presented in these figures. The terms T_1, T_2, T_3, T_4 correspond to the first four vibration periods of the 5MW OWT, i.e., around 4.0s, 0.7s, 0.34s, 0.178s, respectively. $T_{1(z)}$ is 0.153s and refers to the first vertical vibration mode. As shown in Figure 10(a & d), there is a prominent first mode excitation and weaker vertical response at the nacelle level for the records that caused the tower failure near the platform, i.e., damage pattern-1. In case of the damage pattern-2 shown in Figure 10(b & e), there is a significant contribution of higher modes (T_2, T_3, T_4) along with the activation of the first vertical mode ($T_{1(z)}$), with prominent spectral amplifications, thus causing failure at the tower top. Figure 10(c & f) associates the damage pattern-3 with the presence of higher modes (T_2, T_3, T_4) and the vertical response ($T_{1(z)}$) which is additionally coupled with two horizontal modes (T_2 and T_3). Notably, records inheriting strong vertical accelerations are the cause of the damage pattern-2 and 3, regardless of the pulse presence. Thus, it implies that tower top response $S_{a,i(Top)}$ is an efficient parameter for evaluating the damage modes and tower failure locations of OWTs subjected to near-fault crustal records with strong vertical ground motions.

5.2.4. Damage modes and OWT specifications

The relation between the tower damage modes, its geometric properties, and the RNA mass has been briefly pointed out in the previous sections. This section extends that observation to understand the implications of the tower slenderness ratio (l/d), the diameter-to-thickness ratio (d/t), and the RNA mass (m_{RNA}) on the collapse behavior of the two OWTs under study. Table 5 presents the l/d and d/t ratios considering the main tower bottom and top diameter with an average wall thickness described earlier in Table 1. The table also shows the m_{RNA} supported by the 2MW and the 5MW OWT, taken as the percentage of the total superstructure mass above the MSL. Both OWTs have identical l/d ratios, however, the d/t ratios are around 37% higher for the 5MW OWT. The higher d/t ratios indicate a thinner wall section, thus, lesser cross-sectional stiffness. Also, the 5MW OWT contains double the m_{RNA}-percentage than the 2MW OWT, resulting in twice as high vibration periods across all modes as shown in Table 3.

TABLE 5 Damage in relation to l/d ratio, d/t ratio, and m_{RNA}-percentage

Rated power	Slenderness ratio (l/d)			Diameter-to-thickness ratio (d/t)			RNA mass (m_{RNA})	Damage pattern	Record type
	Bottom	Average	Top	Bottom	Average	Top			
2MW	12.8	15.6	19.8	125	103	81	25 %	1	Set A
5MW	12.9	15.8	20.1	200	163	129	50 %	1, 2, 3	Set A Set B

It is observed that for an average l/d ratio of 15.8 and d/t ratio of 163, OWTs supporting 50% of the total superstructure mass as the RNA are vulnerable to near-fault crustal records with a strong PGV content (> 30cm/s), regardless of the pulse presence. The failure may occur by buckling at the main tower base, around its top or in the middle, depending on the presence of significant vertical accelerations in a record. On the other hand, OWTs with m_{RNA} 25% and stiffer tower cross-section, i.e., 37% lesser d/t ratio, are susceptible to extreme pulse-like records, with the possible failure at the main tower base. Based on these observations, l/d ratio, d/t ratio, and m_{RNA} can be adopted as useful parameters for evaluating the seismic vulnerability of OWTs under pulse-like and non-pulse-like ground motions at the ultimate limit conditions.

5.2.5. Alternative IMs

PGV is further utilized along with PGA, on account of its involvement in the pulse-extraction method and the categorical record selection discussed in the earlier text. PGV and PGA are taken as the geometric mean of all three ground motion components. The regression parameters for $S_a(T_1)$, $S_{a,xyz}(T_1)$, PGA and PGV for the two OWTs at SLS and ULS are detailed in Appendix Table A.4. The cloud results for PGA are not shown here, as it shows a negative correlation with high variability, therefore, deemed an inefficient IM for evaluating the seismic vulnerability of OWTs under and pulse-like and non-pulse-like records. On the contrary, PGV shows relatively improved correlation at SLS and ULS for the two OWTs. The cloud analysis results at ULS only are shown in Figure 11 for brevity. The variability of PGV at Y_{ULS} for the 2MW, $\beta_{Y_{ULS}}|PGV$ is identical to $\beta_{Y_{ULS}}|S_{a,xyz}(T_1)$, however, the correlation ρ is decreased. In case of the 5MW OWT, $\beta_{Y_{ULS}}|PGV$ is slightly higher than $\beta_{Y_{ULS}}|S_{a,xyz}(T_1)$, and the correlation ρ is also increased. Thus, PGV also serves as an adequate IM for evaluating

the seismic performance of OWTs under pulse-like and non-pulse-like records, where *PGV* is used as a criterion for selecting these records.

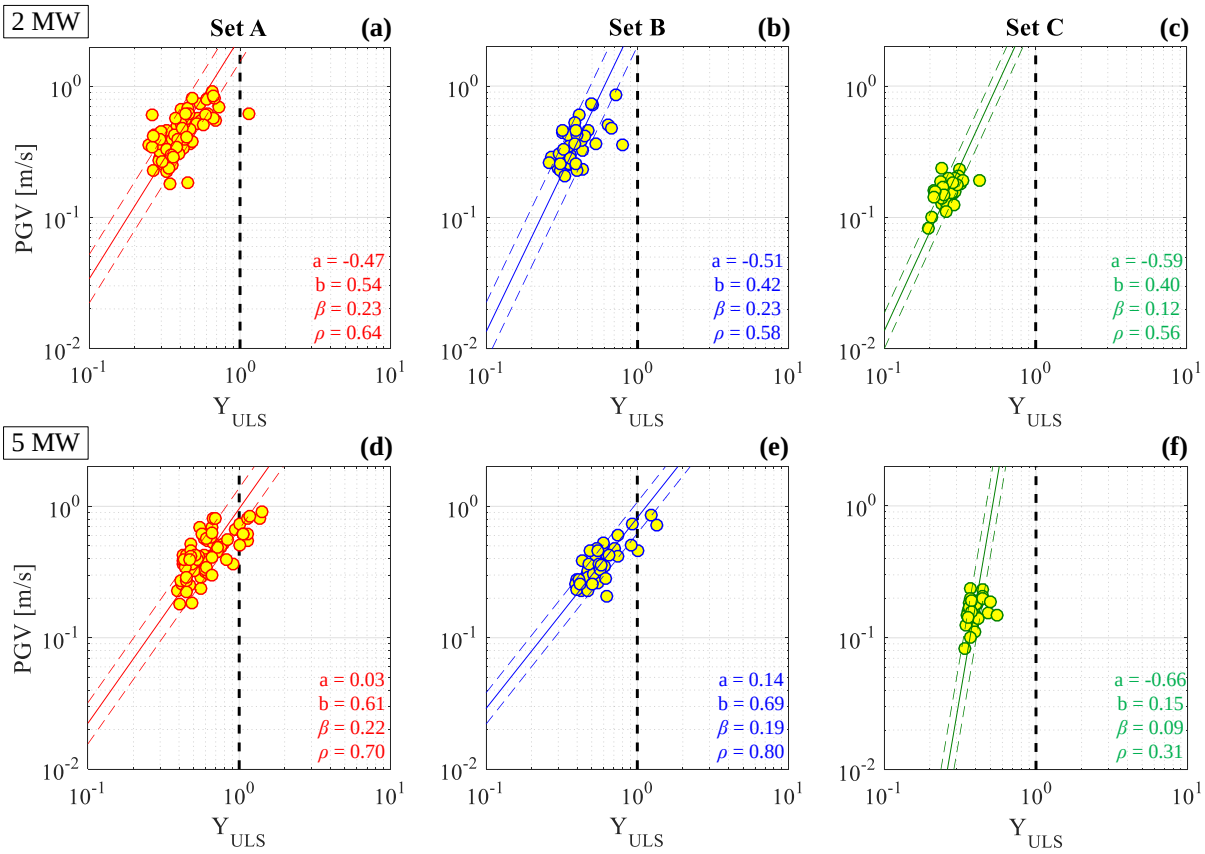

FIGURE 11 Cloud analysis results for *PGV* at ULS

6. FRAGILITY CURVES

Seismic fragility curves are presented to assess the performance exceedance probabilities of 2MW and 5MW OWTs in Figure 12. As discussed earlier, $S_a(T_1)$, $S_{a,xyz}(T_1)$, and *PGV* are efficient *IM*s for evaluating the seismic vulnerability of OWTs under pulse-like and non-pulse-like records containing strong vertical accelerations and the *PGV* content. Figure 12(a to c) shows the seismic fragilities of the two OWTs for $S_a(T_1)$, $S_{a,xyz}(T_1)$, and *PGV* at SLS, respectively. In general, the 5MW OWT has shown more vulnerability to all three sets of records at relatively lower intensity levels for all three *IM*s. This is attributed to the greater tower height, flexibility, and rotor diameter leading to larger wind forces on the 5MW OWT, as highlighted earlier in the cloud analysis. Figure 12(a) shows almost identical fragility curves to all three sets of records, however, both OWTs have shown slightly higher sensitivity to the non-pulse-like records with *PGV* > 30cm/s (Set B). In case of $S_{a,xyz}(T_1)$ shown in Figure 12(b), the 2MW turbine exhibits higher vulnerability to pulse-like (Set A) records because of strong vertical accelerations. For *PGV*, seismic fragilities of both OWTs are different for all three sets of records as shown in Figure 12(c). However, alike $S_a(T_1)$, the turbines have greater susceptibility to Set B records, particularly at 50% probability of exceedance. Figure 12(d to f) presents the fragility curves of the two OWTs at ULS. For all three *IM*s, the 2MW OWT have shown low probabilities of failure for all three sets of records. However, the turbine may collapse under extreme pulse-like (Set A) records as shown in Figure 12(d). Similarly, the 5MW OWT is more prone to fail under pulse-like records but given the presence of strong vertical accelerations and *PGV*>30 cm/s, non-pulse-like records may also increase the failure probability of the OWT as shown in Figure 12(e & f).

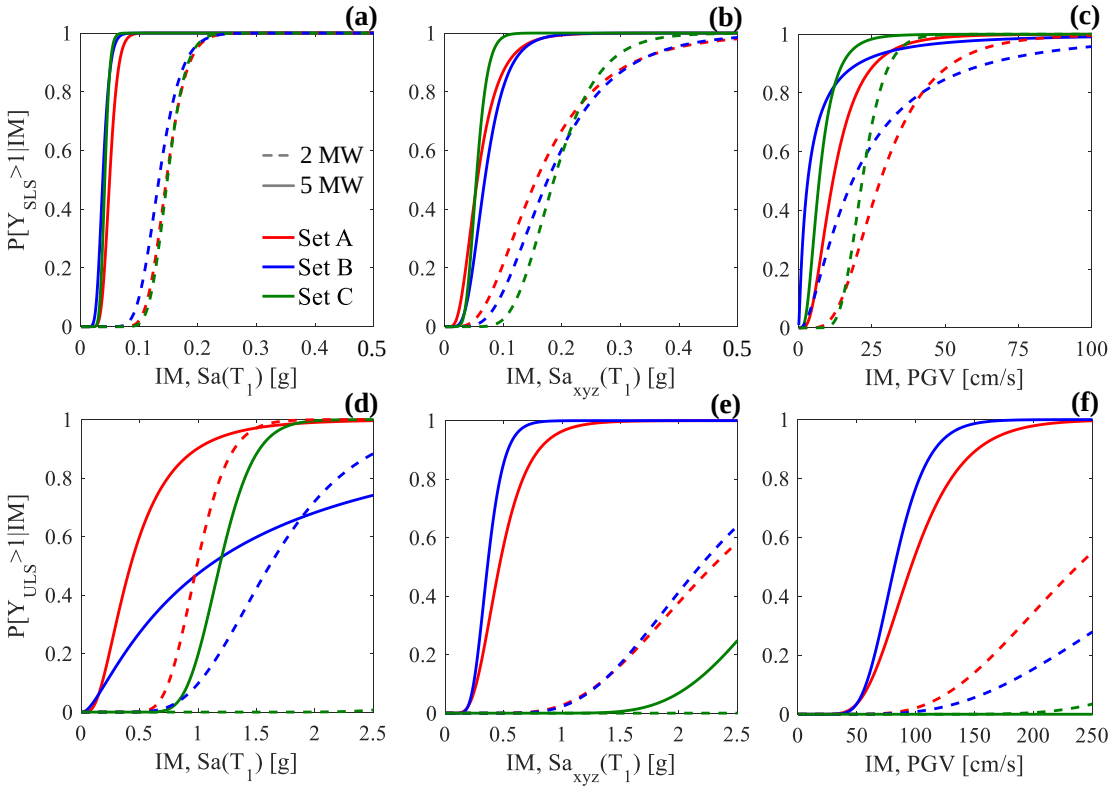

FIGURE 12 SLS and ULS related-fragility curves for 2MW and 5MW at alternative *IMs*. (a & d) $S_a(T_1)$; (b & e) $S_{a,xyz}(T_1)$; (c & f) *PGV*

7. CONCLUSIONS

The study investigates the seismic vulnerability of offshore wind turbines (OWTs) under pulse-like and non-pulse-like records using the performance-based earthquake engineering approach. Two wind turbines of different capacities, i.e. 2MW and 5MW, are considered to examine the differences in their seismic performances. Near-fault shallow crustal records are selected to perform nonlinear dynamic analysis using OpenSees. The records are classified into three sets based on the *PGV* content and pulse presence, such that Set A contains pulse-like records, Set B and C comprise non-pulse-like records with an average *PGV* greater and less than 30cm/s, respectively. Cloud-based fragility assessment is performed to evaluate the velocity pulse effects and scrutinize an efficient choice of intensity measure (*IM*) for OWTs at serviceability limit state (SLS) and ultimate limit state (ULS). Tower stresses and tower top response $S_{a,i(Top)}$ are systematically examined to evaluate the type and location of the damage modes. The conclusions drawn from this study are as follows:

1. Cloud analysis shows the first-mode spectral acceleration $S_a(T_1)$ as an efficient *IM* for OWTs, with prominent higher-mode response, at SLS and ULS. Both OWTs are vulnerable to all three sets of crustal records at SLS. However, the 5MW turbine supporting 50% of the total superstructure mass as the rotor-nacelle-assembly (m_{RNA}) showed higher susceptibility to deform than 2MW OWT with m_{RNA} equivalent to 25%. At ULS, the 2MW OWT is sensitive to extreme pulse-like records only, whereas the 5MW OWT is vulnerable to both pulse-like (Set A) and non-pulse-like records with the mean *PGV*>30cm/s (Set B).
2. $S_{a,xyz}(T_1)$ can be an alternative to $S_a(T_1)$, at ULS, especially when the records used for the nonlinear dynamic analysis contain strong vertical ground motion component. *PGV* also serves as an adequate *IM* for seismic performance evaluation of OWTs under pulse-like and non-pulse-like records, if used as a criterion for the record selection.
3. Buckling dictates the collapse limit for the OWTs. Three tower damage modes, termed as damage pattern-1, 2 and 3, are identified in this study. The first refers to the failure at the main tower base near the platform level. The second is the failure in the vicinity of the RNA at the top, and the third indicates the failure in the upper half of the main tower.
4. The tower top response spectra $S_{a,i(Top)}$ is an efficient parameter for evaluating the damage modes and their locations. It shows that the turbines which tend to fail at the tower base exhibit significant first-mode responses for the records with a weak vertical component. In case of failures occurring around the middle

and tower top, the turbine shows higher mode vibrations coupled with the vertical mode excitation for the records inheriting strong vertical accelerations.

5. RNA mass (m_{RNA}), tower slenderness (l/d) and the diameter-to-thickness ratio (d/t) are useful parameters for assessing the failure modes of OWTs under pulse-like and non-pulse-like records. The 5MW OWT with 50% m_{RNA} and an average l/d and d/t ratio of 15.8 and 163, respectively, is prone to collapse by all three damage modes under all three sets of crustal records. On the contrary, the 2MW OWT with 25% m_{RNA} and stiffer tower sections may fail at the tower base when subjected to extreme pulse-like records only. A detailed parametric study in the future will further enhance the reliability of these parameters in assessing the failure of OWTs.
6. Fragility curves indicate higher vulnerability of the 5MW turbine than the 2MW at both SLS and ULS. For the three *IM*s, particularly at ULS, the 2MW OWT showed low probabilities of failure for all three sets of records. In contrast, the 5MW revealed higher probabilities of failure under near-fault crustal records with strong *PGV* content (>30cm/s) and vertical accelerations, regardless of the pulse presence.

It is important to underline that in this study; the cloud analysis does not consider the effects of the pulse period (T_p). A rigorous investigation is further required to evaluate its influence on the seismic vulnerability assessment of OWTs, whose higher modes contribute significantly to their dynamic behavior.

ACKNOWLEDGEMENTS

Ground motion data for earthquakes, considered in this study, were obtained from the K-NET and KiK-net database (http://www.kyoshin.bosai.go.jp/), the SK-net (http://www.sknet.eri.u-tokyo.ac.jp/), and the PEER-NGA database (http:// peer.berkeley.edu/nga/index.html). This work was carried out using the computational facilities of the Advanced Computing Research Centre, University of Bristol (http://www.bris.ac.uk/acrc/).

REFERENCES

1. Edenhofer O, Pichs-Madruga R, Sokona Y, Seyboth K, Eickemeier P, Matschoss P, *et al. Direct Solar Energy*. 2011.
2. Yang J, Liu Q, Li X, Cui X. Overview of wind power in China: Status and future. *Sustainability (Switzerland)* 2017; **9**(8): 1–12.
3. Witcher D. Seismic analysis of wind turbines in the time domain. *Wind Energy* 2005; **8**(1): 81–91.
4. Prowell I, Veletzos M, Elgamal A, Restrepo J. Experimental and numerical seismic response of a 65 kW wind turbine. *Journal of Earthquake Engineering* 2009; **13**(8): 1172–1190.
5. Prowell I, Uang CM, Elgamal A, Luco JE, Guo L. Shake Table Testing of a Utility-Scale Wind Turbine 2012; **138**(July): 900–909.
6. Kim DH, Lee SG, Lee IK. Seismic fragility analysis of 5MW offshore wind turbine. *Renewable Energy* 2014; **65**: 250–256.
7. Zheng XY, Li H, Rong W, Li W. Joint earthquake and wave action on the monopile wind turbine foundation: An experimental study. *Marine Structures* 2015; **44**: 125–141.
8. Alati N, Failla G, Arena F. Seismic analysis of offshore wind turbines on bottom-fixed support structures. *Phil Trans R Soc A* 2015; **373**(2035): 20140086.
9. IEC 61400-3. *Wind Turbines-Part 3: Design Requirements for Offshore Wind Turbines*. International Electrotechnical Commission Geneva, Switzerland; 2009.
10. DNV GL. *Design of Offshore Wind Turbine Structures (DNV-OS-J101)*. 2014.
11. DNV/Risø. *Guidelines for Design of Wind Turbines*. 2nd ed. Det Norske Veritas and Wind Energy Department, Risø National Laboratory; 2002.
12. De Risi R, Bhattacharya S, Goda K. Seismic performance assessment of monopile-supported offshore wind turbines using unscaled natural earthquake records. *Soil Dynamics and Earthquake Engineering* 2018; **109**: 154–172.
13. Kalkan E, Kunnath SK. Effects of fling step and forward directivity on seismic response of buildings. *Earthquake Spectra* 2006; **22**(2): 367–390.
14. Baker JW. Quantitative classification of near-fault ground motions using wavelet analysis. *Bulletin of the Seismological Society of America* 2007; **97**(5): 1486–1501.
15. Shahi SK, Baker JW. An efficient algorithm to identify strong-velocity pulses in multicomponent ground motions. *Bulletin of the Seismological Society of America* 2014; **104**(5): 2456–2466.
16. Sadowski AJ, Camara A, Málaga-Chuquitaype C, Dai K. Seismic analysis of a tall metal wind turbine support tower with realistic geometric imperfections. *Earthquake Engineering & Structural Dynamics*

2017; **46**(2): 201–219.
17. Somerville PG, Smith NF, Graves RW, Abrahamson NA. Modification of empirical strong ground motion attenuation relations to include the amplitude and duration effects of rupture directivity. *Seismological Research Letters* 1997; **68**(1): 199–222.
18. Bolt, B. A. and Abrahmson N. Estimation of strong seismic ground motions. *International Handbook of Earthquake and Engineering Seismology* 2003: 983–1001.
19. Mimoglou P, Psycharis IN, Ta IM. Computational Methods in Earthquake Engineering 2017; **44**.
20. Zhai C, Chang Z, Li S, Chen ZQ, Xie L. Quantitative identification of near-fault pulse-like ground motions based on energy. *Bulletin of the Seismological Society of America* 2013; **103**(5): 2591–2603.
21. Chang Z, Sun X, Zhai C, Zhao JX, Xie L. An improved energy-based approach for selecting pulse-like ground motions. *Earthquake Engineering & Structural Dynamics* 2016; **45**(14): 2405–2411.
22. Mavroeidis GP, Dong G, Papageorgiou AS. Near-fault ground motions, and the response of elastic and inelastic single-degree-of-freedom (SDOF) systems. *Earthquake Engineering & Structural Dynamics* 2004; **33**(9): 1023–1049.
23. Mimoglou P, Psycharis IN, Taflampas IM. Determination of the Parameters of the Directivity Pulse Embedded in Near-Fault Ground Motions and Its Effect on Structural Response. *Computational Methods in Earthquake Engineering*, Springer; 2017.
24. Tothong P, Cornell CA. Structural performance assessment under near-source pulse-like ground motions using advanced ground motion intensity measures. *Earthquake Engineering & Structural Dynamics* 2008; **37**(7): 1013–1037.
25. Cao Y, Mavroeidis GP, Meza-Fajardo KC, Papageorgiou AS. Accidental eccentricity in symmetric buildings due to wave passage effects arising from near-fault pulse-like ground motions. *Earthquake Engineering & Structural Dynamics* 2017; **46**(13): 2185–2207.
26. Liossatou E, Fardis MN. Near-fault effects on residual displacements of RC structures. *Earthquake Engineering & Structural Dynamics* 2016; **45**(9): 1391–1409.
27. Krawinkler H, Medina R, Alavi B. Seismic drift and ductility demands and their dependence on ground motions. *Engineering Structures* 2003; **25**(5): 637–653.
28. Baker JW, Cornell CA. Vector-valued intensity measures incorporating spectral shape for prediction of structural response. *Journal of Earthquake Engineering* 2008; **12**(4): 534–554.
29. Alonso-Rodríguez A, Miranda E. Assessment of building behavior under near-fault pulse-like ground motions through simplified models. *Soil Dynamics and Earthquake Engineering* 2015.
30. Quiroz-Ramirez A, Arroyo D, Teran-Gilmore A, Ordaz M. Evaluation of the Intensity Measure Approach in Performance-Based Earthquake Engineering with Simulated Ground Motions. *Bulletin of the Seismological Society of America* 2014; **104**(2): 669–683.
31. Ebrahimian H, Jalayer F, Lucchini A, Mollaioli F, Manfredi G. Preliminary ranking of alternative scalar and vector intensity measures of ground shaking. *Bulletin of Earthquake Engineering* 2015; **13**(10): 2805–2840.
32. Iervolino I, Manfredi G. A review of ground motion record selection strategies for dynamic structural analysis. *Modern Testing Techniques for Structural Systems*, Springer; 2008.
33. Kohrangi M, Bazzurro P, Vamvatsikos D, Spillatura A. Conditional spectrum-based ground motion record selection using average spectral acceleration. *Earthquake Engineering & Structural Dynamics* 2017; **46**(10): 1667–1685.
34. Kohrangi M, Vamvatsikos D, Bazzurro P. Pulse-like versus non-pulse-like ground motion records: Spectral shape comparisons and record selection strategies. *Earthquake Engineering & Structural Dynamics* 2018: 1–19.
35. Jonkman J, Musial W. *Offshore code comparison collaboration (OC3) for IEA Wind Task 23 offshore wind technology and deployment*. 2010.
36. Jalayer F, Ebrahimian H, Miano A, Manfredi G, Sezen H. Analytical fragility assessment using unscaled ground motion records. *Earthquake Engineering and Structural Dynamics* 2017; **46**(15): 2639–2663.
37. Arany L, Bhattacharya S, Macdonald JHGG, Hogan SJ. Closed form solution of Eigen frequency of monopile supported offshore wind turbines in deeper waters incorporating stiffness of substructure and SSI. *Soil Dynamics and Earthquake Engineering* 2016; **83**: 18–32.
38. Jonkman J, Butterfield S, Musial W, Scott G. Definition of a 5-MW Reference Wind Turbine for Offshore System Development 2009(February).
39. McKenna F. OpenSees: a framework for earthquake engineering simulation. *Computing in Science & Engineering* 2011; **13**(4): 58–66.
40. Batdorf SB. A Simplified Method of Elastic-Stability Analysis for Thin Cylindrical Shells I - Donnell's Equation. *NACA Technical Note 1341* 1947.
41. API. Recommended Practice for Planning , Designing and Constructing Fixed Offshore Platforms — Working Stress Design. *Api Recommended Practice* 2007; **24-WSD**(December 2000): 242.

42. Mosher RL. *Load-Transfer Criteria for Numerical Analysis of Axially Loaded Piles in Sand. Part 1. Load-Transfer Criteria.* 1984.
43. Vijivergiya VN. Load-movement characteristics of piles. *4th Symp. of Waterway, Port, Coastal and Occean Div., ASCE*, vol. 2, 1977.
44. Maniaci DC, Li Y. Investigating the influence of the added mass effect to marine hydrokinetic horizontal-axis turbines using a general dynamic wake wind turbine code. *Marine Technology Society Journal* 2012; **46**(4): 71–78.
45. ASCE/SEI 7-10. Minimum Design Loads for Buildings and Other Structures: Second Printing 2010.
46. IEC 61400-1. *Wind Turbines-Part 1: Design Requirements*. International Electrotechnical Commission Geneva, Switzerland; 2005.
47. Arany L, Bhattacharya S, Macdonald J, Hogan SJ. Design of monopiles for offshore wind turbines in 10 steps. *Soil Dynamics and Earthquake Engineering* 2017; **92**(September 2016): 126–152.
48. Frohboese P, Schmuck C. Thrust coefficients used for estimation of wake effects for fatigue load calculation. *European Wind Energy Conference*, 2010.
49. Mylona EK V., Sextos AG, Mylonakis GE. Rotational seismic excitation effects on CIDH pile-supported bridge piers. *Engineering Structures* 2017; **138**: 181–194.
50. Bisoi S, Haldar S. Design of monopile supported offshore wind turbine in clay considering dynamic soil-structure-interaction. *Soil Dynamics and Earthquake Engineering* 2015; **73**: 103–117.
51. Golafshani AA, Bagheri V, Ebrahimian H, Holmas T. Incremental wave analysis and its application to performance-based assessment of jacket platforms. *Journal of Constructional Steel Research* 2011; **67**(10): 1649–1657.
52. EN 1993-1-6. Eurocode 3: Design of Steel Structures-Part 1-6: Strength and Stability of Shell Structures 2007.
53. Gere JM, Goodno BJ. *Mechanics of Materials*. 8th ed. Cengage Learning, Boston, MA; 2012.
54. Katsanos EI, Sextos AG, Manolis GD. Selection of earthquake ground motion records: A state-of-the-art review from a structural engineering perspective. *Soil Dynamics and Earthquake Engineering* 2010; **30**(4): 157–169.
55. Foulser-Piggott R, Goda K. Ground-motion prediction models for arias intensity and cumulative absolute velocity for Japanese earthquakes considering single- station sigma and within-event spatial correlation. *Bulletin of the Seismological Society of America* 2015.
56. Dickinson BW, Gavin HP. Parametric statistical generalization of uniform-hazard earthquake ground motions. *Journal of Structural Engineering* 2010; **137**(3): 410–422.
57. Kaynia AM. Seismic considerations in design of offshore wind turbines. *Soil Dynamics and Earthquake Engineering* 2018(September 2017): 0–1.
58. Katsanos EI, Sanz AA, Georgakis CT, Thöns S. Multi-hazard response analysis of a 5MW offshore wind turbine. *Procedia Engineering* 2017; **199**: 3206–3211.
59. Prowell I, Elgamal A, Uang C, Jonkman J. Estimation of seismic load demand for a wind turbine in the time domain. *European Wind Energy Conference (EWEC), Warsaw, Poland, Apr*, 2010.
60. Kuramoto H. Seismic Design Codes for Buildings in Japan. *Journal of Disaster Research* 2003; **1**(3): 341–356.
61. *Eurocode 8: Design of structures for earthquake resistance-Part 1: General rules, seismic actions and rules for buildings*. 1998.
62. TSDC. Regulations for buildings to be constructed in earthquake prone areas. *Turkish Seismic Design Code, Ankara, Turkey* 2007.
63. NTC2008 - Norme tecniche per le costruzioni - D.M. 14 Gennaio 2008 (D.M. 4/2/08).
64. Katsanos EI, Thöns S, Georgakis CT. Wind turbines and seismic hazard: a state-of-the-art review. *Wind Energy* 2016; **19**(11): 2113–2133.
65. Mazzoni S, Mckenna F, Scott MH, Fenves GL, Iii A. *Open System for Earthquake Engineering Simulation (OpenSees) OpenSees Command Language Manual*. 2006.
66. Mollaioli F, Lucchini A, Cheng Y, Monti G. Intensity measures for the seismic response prediction of base-isolated buildings. *Bulletin of Earthquake Engineering* 2013; **11**(5): 1841–1866.
67. Filippou FC, Bertero VV, Popov EP. Effects of bond deterioration on hysteretic behavior of reinforced concrete joints 1983.
68. Zhao Z, Dai K, Camara A, Bitsuamlak G, Sheng C. Wind Turbine Tower Failure Modes under Seismic and Wind Loads. *Journal of Performance of Constructed Facilities* 2019; **33**(2): 04019015.